

A Mechanically Flexible, Implantable Neural Interface for Computational Imaging and Optogenetic Stimulation over $5.4 \times 5.4 \text{ mm}^2$ FoV

Sajjad Moazeni, *Member, IEEE*, Eric H. Pollmann, *Student Member, IEEE*, Vivek Boominathan, *Member, IEEE*, Filipe A. Cardoso, Jacob T. Robinson, *Senior Member, IEEE*, Ashok Veeraraghavan, *Senior Member, IEEE*, and Kenneth L. Shepard, *Fellow, IEEE*

Abstract—Emerging optical functional imaging and optogenetics are among the most promising approaches in neuroscience to study neuronal circuits. Combining both methods into a single implantable device enables all-optical neural interrogation with immediate applications in freely-behaving animal studies. In this paper, we demonstrate such a device capable of optical neural recording and stimulation over large cortical areas. This implantable surface device exploits lens-less computational imaging and a novel packaging scheme to achieve an ultra-thin ($250 \mu\text{m}$ -thick), mechanically flexible form factor. The core of this device is a custom-designed CMOS integrated circuit containing a 160×160 array of time-gated single-photon avalanche photodiodes (SPAD) for low-light intensity imaging and an interspersed array of dual-color (blue and green) flip-chip bonded micro-LED (μLED) as light sources. We achieved $60 \mu\text{m}$ lateral imaging resolution and 0.2 mm^3 volumetric precision for optogenetics over a $5.4 \times 5.4 \text{ mm}^2$ field of view (FoV). The device achieves a 125-fps frame-rate and consumes 40mW of total power.

Index Terms—all-optical neural interface, computational imaging, lens-less imager, SPAD, optogenetics, flexible packaging

I. INTRODUCTION

Recent advancements in optical functional imaging and optogenetics have brought us closer to deciphering the human brain and inventing the next-generation of brain-computer interfaces (BCI). The advent of genetically encoded calcium and voltage indicators (GECI/GEVI) and optogenetic probes has unlocked new capabilities for intracellular recording *in-vivo* with near single-action-potential sensitivity and for stimulation with cell-type specificity [1]. Combining both optical functional imaging and optogenetics into a single device

enables simultaneous, all-optical, neural interrogation with the potential to revolutionize neuroscience studies. However, these methods are relegated today largely to expensive microscopes based on free-space optics. Miniaturizing such microscopes into an implantable form factor remains an elusive goal. As a first step towards developing such a device, a variety of head-mounted “miniscopes” have been demonstrated [2]–[4]. Using conventional lens-based optics, however, these devices require considerable volume (more than 2 cm^3) to support field of views (FoVs) in the mm^2 range. Because of the trade-off between the lens size and FoV in lens-based imagers [5], [6], imaging larger FoVs comes at the cost of much larger device size. For instance, achieving a $7.8 \times 4 \text{ mm}^2$ FoV in a miniscope required a volume of over 24 cm^3 and mass of 33g [3]. Additionally, state-of-the-art miniscopes either lack or have very limited optogenetic capabilities for stimulation with any spatial selectivity [7]. To build a fully implantable miniscope, a more volume-efficient device is necessary that spans a relatively large cortical area while maintaining a minimally-invasive form factor. We have previously laid out a vision of what might be possible with whole new class of implantable optoelectronic devices [8].

In this paper, we demonstrate a new device ultimately capable of such a fully implantable form factor that supports all-optical neural recording and stimulation over a $5.4 \times 5.4 \text{ mm}^2$ FoV at the target cortical depths of up to $200 \mu\text{m}$ (Layer 2/3 in mouse brain). This mechanically flexible, implantable brain-surface device, illustrated in Fig. 1, enables fluorescence imaging in an ultra-thin ($< 250 \mu\text{m}$ -thick) form factor by exploiting a recently developed lens-less computational imaging approach [6]. Device functionality is provided by a die-thinned CMOS integrated circuit consisting of a 2D array of SPAD detectors and flip-chip bonded μLED light emitters for both fluorescence excitation and optogenetic stimulation. While the proof-of-concept device developed is wired, the ultimate incarnation of this device will be interfaced wirelessly, as shown in Fig. 1.

This paper is organized as follows: Section II describes system-level design considerations for an all-optical neural interface. Section III introduces the computational imaging method. Chip architecture and packaging are presented in Section IV and Section V, respectively. Experimental results are

This work was supported in part by DARPA NESD under Contract N66001-17-C-4012 and by the National Science Foundation under Grant 1706207. (S. Moazeni and E. H. Pollmann, are co-first authors.)

Sajjad Moazeni was with Columbia University, New York, NY 10027 USA. He is now with the University of Washington, Seattle, WA 98195 USA (e-mail: smoazeni@uw.edu).

Eric H. Pollmann, Filipe A. Cardoso, and Kenneth L. Shepard are with Columbia University, New York, NY 10027 USA. (e-mail: {ehp2121, fa2495}@columbia.edu, shepard@ee.columbia.edu).

Vivek Boominathan, Jacob T. Robinson, and Ashok Veeraraghavan are with Rice University, Houston, TX 02215 USA. (e-mail: vivek.booms@gmail.com, {jtrobinson, vashok}@rice.edu).

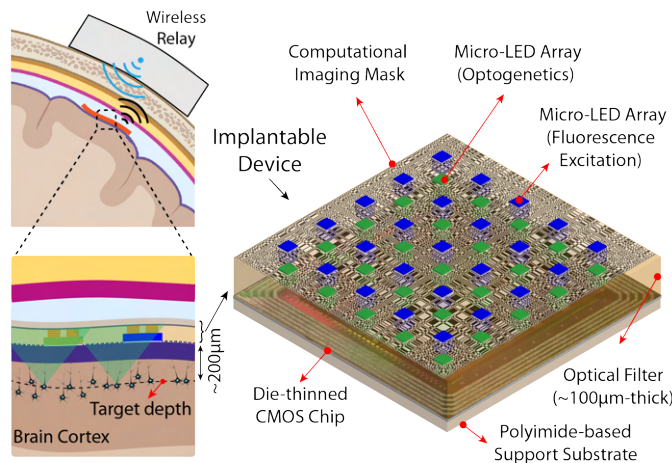


Fig. 1. Proposed mechanically flexible and implantable device for all-optical neural recording and stimulation.

discussed in Section VI and compared with prior work in the conclusion (Section VII).

II. DESIGNING AN IMPLANTABLE ALL-OPTICAL NEURAL INTERFACE

In this section, we present an overview of design considerations and requirements for an implantable optical neural interface device for fluorescence imaging and optogenetics. The ideal form factor for such a device is one that is ultra-thin, flexible, and fully wireless with low enough power consumption to keep device heating below $\sim 1^\circ\text{C}$. Fig. 1 illustrates such a device, which can cover large cortical areas and target depths up to $\sim 200\mu\text{m}$ with both epi-fluorescence imaging and stimulation capability. We elaborate on various aspects of the design in the following subsections.

A. Integrated Light Sources

A fully implantable device must contain all the necessary light emitters for fluorescence excitation and optogenetics that are also capable of reaching the entire FoV with sufficient brightness and spatial selectivity at the target depth. Lasers are typically used in bench-top optical imaging and optogenetics experiments. While continuous-wave (CW) visible light lasers have been previously integrated in a brain implant for optogenetic stimulation [9], poor efficiencies (typically 10%) and the need for an active photonic platform to steer highly focused laser beam to illuminate large FoVs make lasers largely unsuitable for low-power and fully implanted optical neural interfaces. Alternatively, μLED arrays show great promise to create high-density and programmable illumination patterns. However, monolithic GaN [10], [11] are not CMOS compatible, and organic LEDs (OLED) [12], [13] do not yet provide sufficient brightness for fluorescent imaging or stimulation. As a result, we use flip-chip bonded arrays of commercial Cree μLED s [14] in this work. Despite their relatively larger footprint ($220\mu\text{m} \times 250\mu\text{m}$) compared with monolithic GaN and OLEDs, they provide ultrahigh brightness at high efficiency ($\sim 30\%$) and relatively narrow linewidth ($\sim 20\text{nm}$).

Our device incorporates two separate 5×5 arrays of blue (470nm) and green (535 nm) TR2227 Cree μLED s with 1.08mm pitch for fluorescence excitation and optogenetic stimulation, respectively, as shown in Fig. 1. We will discuss the impacts of missing imager pixels due to μLED placements in Section III. The choice of these wavelengths depends on the target optogenetic and fluorescent probes [1]. In order to estimate the brightness at our target depth ($\sim 200\mu\text{m}$), we modeled the light propagation of μLED s in scattering tissue using Monte Carlo methods [15]. We used typical values of optical properties for the brain tissue (scattering and absorption coefficients of $\mu_s = 10\text{mm}^{-1}$ and $\mu_a = 0.01\text{mm}^{-1}$, respectively, scattering anisotropy of $g = 0.9$, and refractive index of $n = 1.38$ [16]). Fig. 2 shows the simulation results of a 2-by-2 subset of our μLED array. Green μLED s with maximum radiance of 12mW result in the brightness of $\sim 114\text{mW}/\text{mm}^2$ at the brain surface. After propagation in $200\mu\text{m}$ brain tissue, the brightness drops to $\sim 4\text{mW}/\text{mm}^2$ due to the angular spreading, tissue scattering, and absorption (Fig. 2a). Given the minimum required light intensity of $\sim 0.5\text{mW}/\text{mm}^2$ required at the location of neuron for most optogenetic probes [17], our μLED array is sufficiently bright and dense to stimulate the entire FoV at the target depth. On the imaging side, blue μLED s provide a maximum radiance of 30mW equivalent to a power density of $\sim 285\text{mW}/\text{mm}^2$. This results in a minimum fluorescence excitation light intensity of $\sim 10\text{mW}/\text{mm}^2$ at the target imaging depth of $200\mu\text{m}$ while the backscattered excitation light reaches $\sim 10\text{mW}/\text{mm}^2$ at the surface of device, as the simulation shows in Fig. 2b.

B. Optical Filters

We also need to integrate thin and flexible optical filters with sufficient optical density (OD) to reject the excitation light background over the fluorescent emission. Despite prior efforts to integrate interference filters [18] and plasmonic structures [19] with CMOS image sensors, filtering requirements are particularly challenging for our device due to the small Stokes shift of GECI/GEVI biomarkers ($< 30\text{nm}$) [20] compared with fluorophores in other applications ($> 100\text{nm}$) [21].

In order to estimate the signal-to-background ratio (SBR), we use the light propagation model shown in Fig. 2b. The

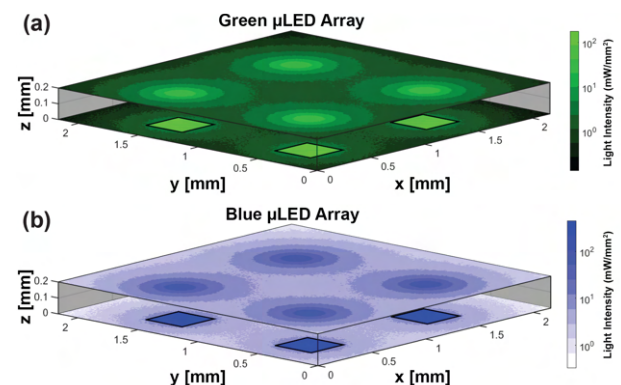


Fig. 2. Light propagation simulation in the brain tissue from (a) blue and (b) green μLED arrays (z denotes the depth into the brain tissue with $z = 0$ corresponding to the device surface).

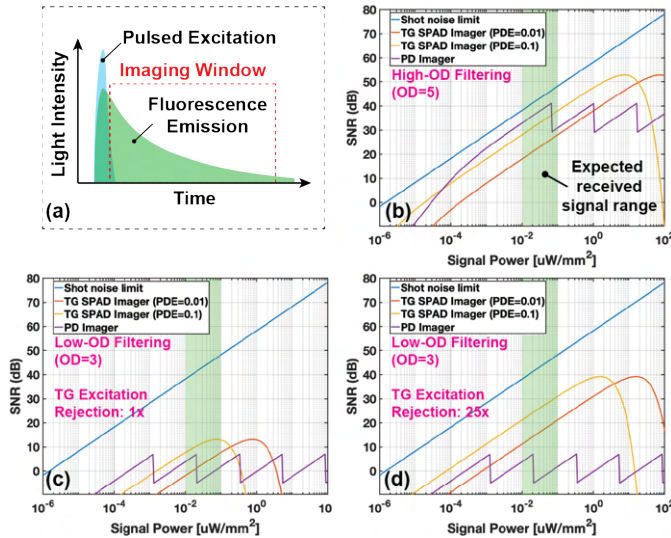


Fig. 3. (a) TG fluorescence imaging, and (b-d) SNR vs. received fluorescent emission light intensity at the imager for multiple conditions.

fluorescence conversion efficiency from blue to green fluorescence emission light (e.g., 518nm which is the peak emission of widely used GCaMP6f) is estimated to be $\sim 0.17\%$ based on the Beer-Lambert law and GCaMP6f's brightness ($3700\text{M}^{-1}\text{mm}^{-1}$ [20]) typical concentration (10^{-6}M [22]), and neuron's diameter ($\sim 20\mu\text{m}$). Assuming isotropic scattered emission and $10\text{mW}/\text{mm}^2$ fluorescence excitation light intensity at the target imaging depth, we expect the received fluorescent emission light intensity of $\sim 0.02\mu\text{W}/\text{mm}^2$ at the device, which results in the peak SBR of 0.2×10^{-5} . This normally necessitates using thick ($>1\text{mm}$) and rigid interference filters on glass with ODs of better than 6 in table-top imaging setups and miniscopes. However, this imposes serious challenges to make an ultrathin and mechanically flexible imager. More importantly, computational imaging, adopted in this work, relies on detecting wide-angle photons to provide large effective numerical aperture (NA). On one hand, interference filters are inherently angle-sensitive, providing peak performance at normal incidence. On the other hand, absorption filters are insensitive to angle, but typically cannot provide more than OD3 of rejection due to their more gradual cutoff slope and autofluorescence effects [23]. To achieve the best filter performance, we combine a wide-angle interference filter, an absorption filter (described in Section V), and time gating (TG) to achieve a total peak filter performance of better than OD5.

C. Image Sensor

Miniscopes and miniaturized cameras use commercial image sensors with arrays of photo diodes (PDs) fabricated in CMOS imager (CIS) processes. Instead, we design and optimize a custom SPAD-based image sensor to enable TG fluorescence imaging through single-photon counting. In gated operation, the imager is only activated after each excitation pulse, as illustrated in Fig. 3a. Gating the sensor provides additional background rejection of scattered excitation light complementing the interference and absorption filters. Moreover, it also enables a

fluorescence life-time imaging (FLIM) mode [24], [25].

While TG imaging can, in principle, provide arbitrarily large excitation rejections, the efficacy is limited in practice by the turn-off time of the excitation pulse (the more abrupt the turn-off, the better), the fluorescence life-time (longer lifetimes provide easier background rejection), and the impulse-response function (IRF) of the SPAD detectors (the faster the IRF, the better). Despite the advantage of having no read noise, SPAD-based imagers suffer from lower photon detection efficiencies (PDE) when compared to conventional PD imagers. Additionally, TG imagers typically consume larger power compared with PD or passive SPAD imagers due to the extra dynamic power required for gating the pixels. In order to contrast the overall performance of a SPAD-based TG imager with a conventional PD-based imager, we have modeled and calculated SNR [26], [27] for both imager types. The PD imager parameters (quantum efficiency (QE) of 0.6, well capacity of 52ke^- , dark current of 0.15fA , and read noise of 10e^-) are based on a commercial Aptina CMOS image sensor (MT9V021) [2], while we assumed a conservative dead-time of 25ns and dark-count-rate of 26cps for the SPADs. We look at two PDE possibilities for the SPAD imager, 1% and 10% , as determined by both fill factor (FF) and photon detection probability (PDP). Both SPAD and PD imagers contain photon shot noise due to the background and fluorescence counts as well as dark-counts, while the PD imager has additional read noise. Shot noise limit curves in Fig. 3 indicate the theoretical SNR limit of imaging fluorescence with no background and the noise floor is entirely determined by photon shot noise.

At high intensities, saturation is determined by full well capacity in the PD imager and by the dead-time in the SPAD imager. The dynamic range of the PD imager is extended through multiple sampling in which the frame window is divided into k samples at $1/2^k$ fractions of the starting integration time, such that well saturation is avoided for the shortest integration-time sample. The total frame time (sum of all integration time of the k samples) is set to $1/f$, where f is the frame rate. The resulting SNR of the PD imager in the well-saturated regime is estimated using the multiple sampling scheme [27]. At our target frame-rate of $f=125\text{fps}$ (as required for emerging GEVI reporters which can detect sub-ms action potentials [28]), Fig. 3 shows the SNR as a function of received fluorescence power for three imagers under two filtering scenarios: optical filtering of OD5 (Fig. 3b), and optical filtering of OD3 (Fig. 3c-d). Notice that imagers can become saturated due to the relatively large excitation background intensity. Overall, the TG SPAD-imager can achieve a higher SNR compare with a PD imager for low-OD ($\text{OD} < 3$) filtering, and the improvement is larger at higher TG excitation background rejections (TG of $1\times$ and $25\times$ are plotted in Fig. 3c-d). This results from the challenges PD imagers have in managing the background light. Notice that even increasing the dynamic-range of a PD imager cannot solve this issue as the excitation background and SNR will be limited by the optical filtering OD.

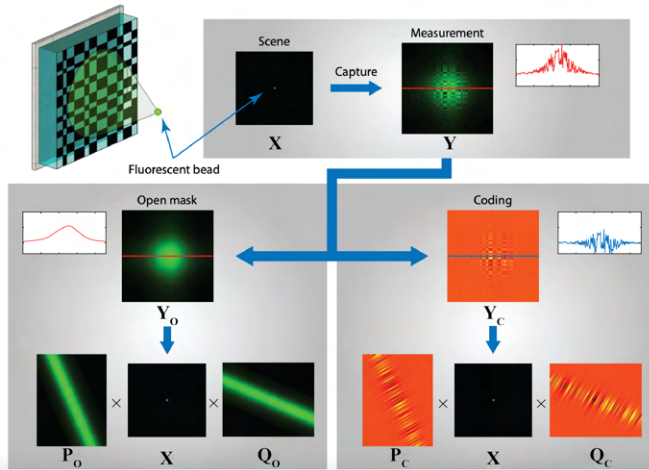


Fig. 4. Texas two-step (T2S) computational imaging model from [6].

At OD 5, however, PD imagers outperform the SPAD-based imagers, mainly because of the lower PDE of SPADs. This can be rectified in the future with larger FF SPAD designs, demonstrated in part by the more comparable performance achieved at 10% PDE for the SPAD-based design in Fig. 3b.

Another critical design consideration is the total power consumption to minimize the heating in brain tissue. As explained in Section VI, our device consumes 45mW total power, estimated to keep tissue heating below $\sim 1.5^\circ\text{C}$ [29]. While it is within the range to enable continuous operation without heating concerns, further low-power optimization can lower the heating to even below the ideal range of 1°C .

III. COMPUTATIONAL IMAGING

Lens-based microscopes suffer from a fundamental trade-off between device size and performance; as lenses become smaller, they must either collect less light or image a smaller FoV [6]. This makes them unsuitable for implantable fluorescence imagers. In this work, we exploit computational imaging [5], [30] to enable a lens-less, compact and ultrathin device. In a lens-based system, the lens collects and focuses light from the scene pixels to the sensor pixels with a one-to-one mapping, but in a computational lens-less system, unfocused light from a single point on the scene is spatially modulated (by the mask) and mapped to multiple sensor pixels. Computational imaging masks can be realized with either a coded-aperture mask [6], phase mask [31] or an arbitrary diffuser mask [30]. After the calibration, the scene is computationally reconstructed by running an inverse imaging algorithm on the raw capture. Additionally, we can reconstruct a 3D scene from a single raw capture by calibrating and solving the optimization problem at multiple depths. In this approach, we can achieve large FoVs (equal to imager's area) with a high effective NA in an ultrathin form factor. This leads to a higher SNR compared with near-field lens-less approaches such as angle-sensitive, metal gratings and plasmonic structures [32], [33]. The lens-less computational imaging in our device is adopted from the Texas two-step (T2S) model [6] and it is described below.

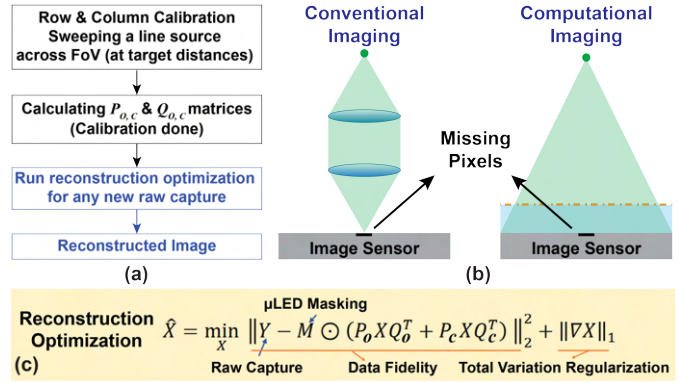


Fig. 5. (a) Computational imaging overall flow, (b) effect of missing pixels on conventional lens-based vs. computational imagers, (c) modified reconstruction optimization problem after incorporating the effect of missing pixels.

A. Texas two-step (T2S) Model

The T2S model [6] requires a coded-aperture mask to spatially encode the unfocused light from the scene comprised of incoherent micron-scale fluorescent sources (e.g., neurons) as shown in Fig. 4. This approach greatly simplifies both the calibration and image reconstruction process by using a separable mask pattern composed of the outer product of two random binary vectors. Despite a simple mask design and fabrication steps (Section V), it improves the computational tractability of reconstruction over other methods using arbitrary diffuser masks [30]. While an amplitude binary mask with overall 50% transmission was used in this work, phase masks can also be used to achieve a higher SNR [31], [34].

B. Image Reconstruction

Figure 4 illustrates the T2S model assuming a single fluorescent bead as the scene. Due to the mask separability, local spatially varying point spread function can be written as the superposition of two independent terms: The first term models the effect of a hypothetical “open” mask (with no apertures), and the second term models the effect due to the coding of mask patterns. Hence, for a 2D (planar) scene X , the raw capture at the imager (Y) can be expressed as:

$$Y = Y_o + Y_c = P_o X Q_o^T + P_c X Q_c^T \quad (1)$$

where P_o and P_c operate only on the rows of X , and Q_o and Q_c operate only on the columns of X (the subscripts o and c refer to “open” and “coding,” respectively). In order to image a 3D volumetric scene from a single shot, we can extend equation (1) to multiple depths as:

$$Y = \sum_{d=1}^D P_{od} X_d Q_{od}^T + P_{cd} X_d Q_{cd}^T \quad (2)$$

where the subscript d represents the depth assuming the entire target 3D volume is discretized over D planar samples. By knowing the $P_{o,c}$ and $Q_{o,c}$ matrices, we can reconstruct the scene from any raw capture by solving a regularized least-squares reconstruction optimization problem (Fig. 5a). The one-time

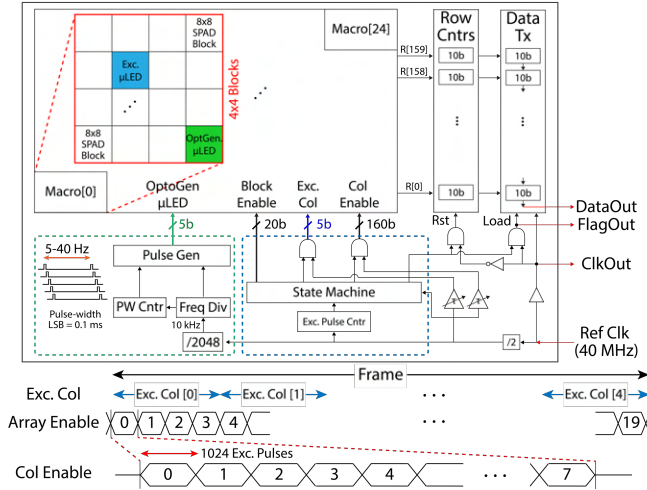


Fig. 6. Block diagram of the all-optical neural interface chip with the timing diagrams of control signals for rolling-shutter imaging and stimulation included (all the control and enable signals are thermometer coded).

calibration process is used to estimate these four calibration matrices ($P_{o,c}$ and $Q_{o,c}$). The calibration process is performed by sweeping the vertical and horizontal fluorescence line source in the row and column directions, respectively, across the entire FoV. This 2D raster-scan procedure is repeated for all D depths (distance above the mask) of interest and essentially the step size of depth scans determines the resolution depth imaging.

C. Computational Imaging with Missing Pixels

Illuminating a large FoV uniformly with sufficient light intensity for implantable optical neural devices is very challenging. Unlike previous efforts to place light source on the boundary of image sensors [34], [35], we are distributing μ LEDs across the entire imager as illustrated in Fig. 1 to solve this issue. However, this μ LED placement will interfere with the imager. Even though the sensor is missing 12.5% of the pixels of a full 160×160 array due to the μ LEDs placement on the chip, the computational lens-less imaging is able to compensate for these “gaps” in image reconstruction. This contrasts with a lens-based imager which would miss all fluorescent sources located above the μ LEDs (Fig. 5b). We exploit this unique advantage of computational imaging by modifying equation (1) as follows:

$$Y = M \odot (P_o X Q_o^T + P_c X Q_c^T) \quad (3)$$

where M is a 160×160 binary matrix with zeros where ever pixels are missing and \odot denotes the element-wise (Hadamard) product. Thus, we used the modified image reconstruction optimization (for a single depth) as shown in Fig. 5c.

IV. CHIP ARCHITECTURE

The all-optical neural interface chip was designed and implemented in a $0.13\text{-}\mu\text{m}$ high-voltage CMOS process. Fig. 6 depicts the chip architecture and imaging timing diagrams. Details of each major sub-block circuitry are described below.

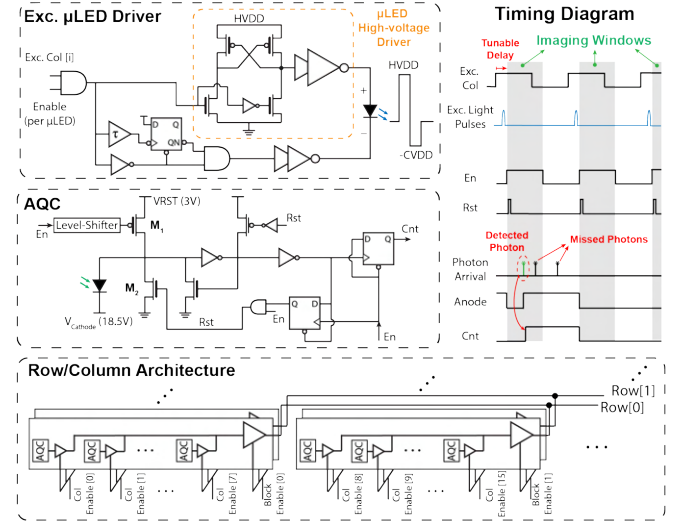


Fig. 7. Circuit diagrams of major sub-blocks including excitation μ LED drivers, AQC, and row/column connectivity architecture with an example timing diagram of photon detection operation.

A. Imager Architecture and Optogenetics Backend

The imager operates in the photon-counting mode with a configurable, sliding time-gate to provide additional background rejection as described in Section II. In order to reduce power, area, and readout data-rate requirements, the imager employs a rolling-shutter which is combined with selective powering of the excitation μ LEDs to reduce power and also help to reduce excitation background. The entire imager is comprised of a 5×5 array of macros, each consisting of 16 blocks in a 4×4 configuration. Of these blocks, 14 are 8×8 SPAD arrays, one is for the excitation μ LED driver, and one is for the optogenetic μ LED driver. During the selection of each sub-frame, which consist of a 5×1 macro column, only excitation μ LEDs in the given column are activated. The SPAD array blocks are enabled column-wise, where each pixel remains active for 1024 excitation pulses of the μ LED, and the detected photon counts are stored in shared-row 10-bit counters. Overall, the imager achieves a frame-rate of 125fps with a 40MHz reference clock. The data transmitter (Tx) block serializes the counter values and sends them off-chip to a control FPGA.

For optogenetics, stimulation signals are generated on-chip with tunable repetition-rates (5-40Hz) and pulse-widths (with 0.1ms LSB precision). The optogenetic μ LED columns are also time-multiplexed to reduce the peak current and required on-chip decoupling capacitance. The stimulation pattern can be configured by enabling individual μ LEDs, each one illuminating $\sim 0.2\text{mm}^3$ brain regions covering the entire FoV with 2D spatial selectivity as simulated in Fig. 2.

B. Micro-LED Drivers

There are two different types of μ LED drivers for optogenetic and fluorescence excitation arrays. Due to slow optogenetic signals, the programmable control signals are generated in the chip periphery and then distributed across each column. Then, the μ LED high-voltage drive head is implemented using a level-

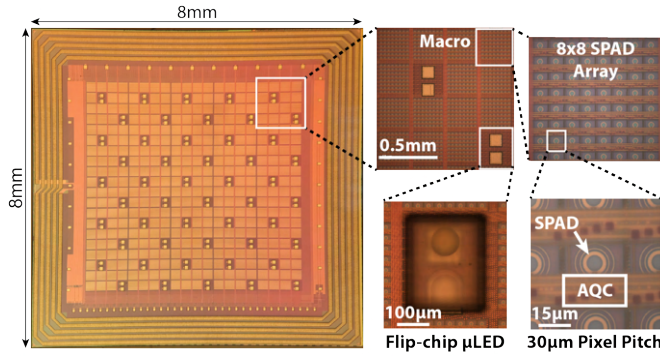


Fig. 8. Micrographs of the bare chip and a flip-chip bonded μ LED.

shifter to apply up to 3.3V to the optogenetic μ LEDs. Each high-swing μ LED driver is also equipped with ~ 0.1 nF of on-chip decoupling capacitance. The driver for the excitation μ LEDs (shown in Fig. 7) is also based on the same high-voltage drive head with additional capabilities to generate sub-ns pulses locally by driving the μ LED cathode to CVDD for turn-off. In doing so, we also push the μ LED into reverse bias, reducing the turn-off time and, consequently, improving the effectiveness of time gating [36].

C. Active Quench and Clock-based Reset Circuit (AQC)

The SPADs are implemented with a 7.5- μ m-diameter active area using a custom implant. Each pixel has a 30 μ m pitch with an AQC and 5% effective FF. The AQC circuit and its timing diagram is illustrated in Fig. 7. The excitation μ LED driver generates ultrashort light pulses at every positive edge of the excitation clock (*Exc. Col*). Next, a delayed clock (*EN*) is used to activate the AQCs for photon detection. On the rising edge of *EN*, a level-shifter turns-off M_1 and triggers a minimum duration one-shot reset pulse to the gate of M_2 . When *ANODE* is

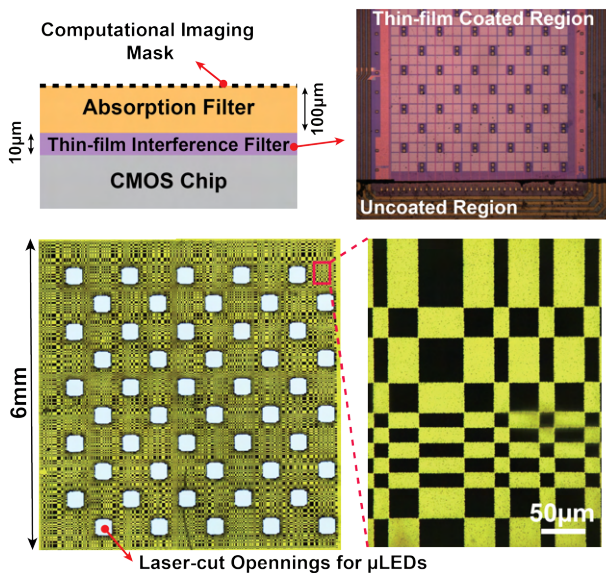


Fig. 9. Cross-section of imager chip with integrated optical filters, micrographs of the chip with interference filter, and the absorption filter with imaging mask fabricated on top.

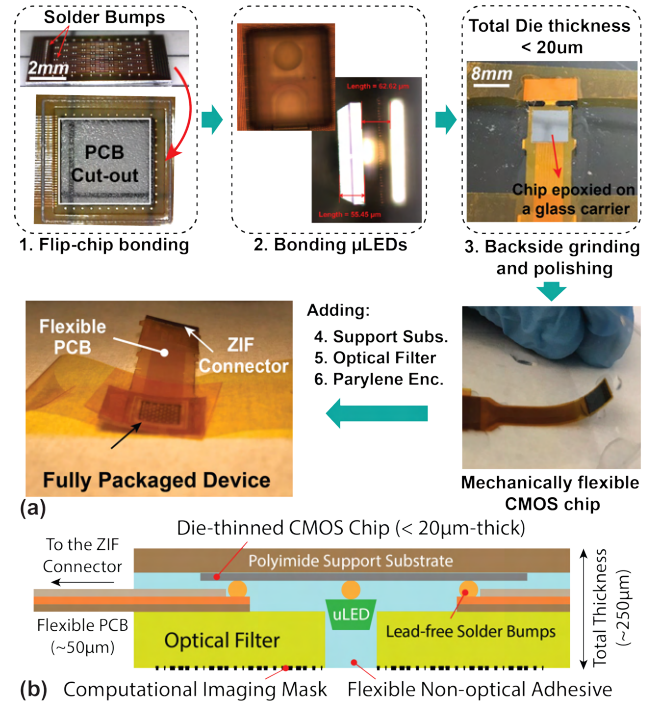


Fig. 10. Flexible packaging: (a) process steps and photos of final device, and (b) final package cross-section (Parylene encapsulation is not shown).

discharged to *GND*, the inverter-based comparator flips its output leaving the SPAD in a high-impedance Geiger-counting mode. Avalanche detection of a photon causes the comparator to flip, which quenches the avalanche current and triggers the buffered output to the row-shared 10b counter.

V. INTEGRATION AND PACKAGING

Micrographs of the chip and major sub-blocks are shown in Fig. 8. The entire chip area is 8 \times 8mm². In this section, we elaborate on the fabrication and post-processing steps of this CMOS chip to make it mechanically flexible, while containing all the crucial components including optical filters and μ LEDs.

A. The Imaging Mask and Optical Filters Fabrication

The binary amplitude mask is fabricated by patterning a 100-nm-thick chromium layer with 15 μ m feature sizes on a 100- μ m-thick flexible absorption filter that is bonded onto the chip. The mask pattern and feature sizes are optimized for a mask-sensor separation and the imaging distance of 100 μ m and 200 μ m, respectively. Fig. 9 shows the cross-section of integrated optical filters and the imaging mask along with some of their micrographs. We employed both a long-pass absorption filter and a custom-designed wide-angle interference filter to reject excitation light scattered from the tissue. The interference filter consists of multiple thin-film dielectric layers with a total thickness of $\sim 10\mu$ m, which is directly deposited on the CMOS chip. This filter is optimized to reject the 470nm excitation light relative to fluorescence emission at 520nm with OD > 3 for angles up to 45°. During the deposition process, bond pads are

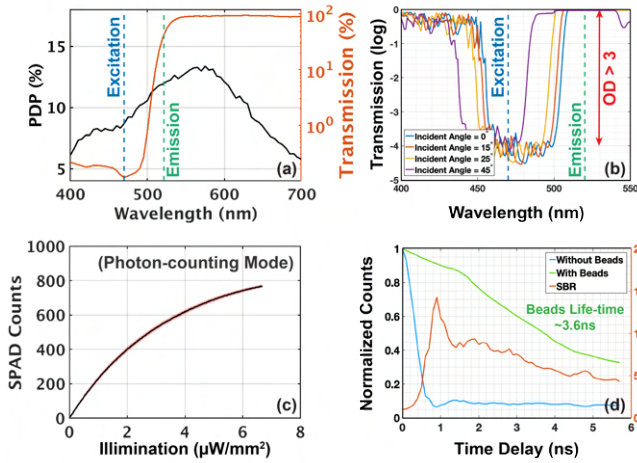


Fig. 11. (a) SPAD's PDP and absorption filter transmission, (b) interference filter transmission, (c) SPAD's non-linear response, and (d) time-gating performance averaged over all pixels.

protected by photoresist and tape, making them accessible after the filter integration for bonding μLEDs .

Unlike angle-sensitive interference filters, the absorption filter accepts wide-angle photons and can be used as the $100\mu\text{m}$ spacer required for the computational mask without increasing the overall thickness of the system. The gelatin-based filter in this work provides $\sim 26\text{dB}$ ($\text{OD}2.6$) and it is also laser cut to create openings for the μLEDs .

B. Flexible Packaging Flow

Future implantable neural interfaces should be mechanically flexible to conform to brain curvatures [37]. This is particularly critical for large surface devices, covering large cortical areas. Here, we describe the packaging approach developed to make our device mechanically flexible, which is achieved by die thinning the CMOS chip down to below $20\mu\text{m}$ total thickness. It has been shown previously that die-thinned CMOS chips can be bent to sub-2-cm radii of curvature with gate delay and drain current changes of less than 7% [38], [39]. While flexible thin-film transistor platforms have been demonstrated recently for biomedical applications [40], [41], they lack the versatility and scalability of CMOS processes.

Fig. 10a shows the full packaging flow developed in this work. After depositing the interference filter on the CMOS chip, the die is flip-chip bonded onto a polyimide flexible PCB with thickness of $\sim 50\mu\text{m}$ with lead-free solder bump (Step 1). The PCB has a cut-out to provide a viewing window for the chip while maintaining sufficient overlap with chip boundary for

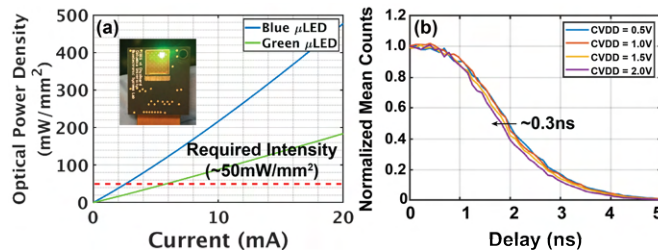


Fig. 12. The μLEDs optical power density (a) and the measured time-gated optical IRF using the chip itself at multiple CVDD (b).

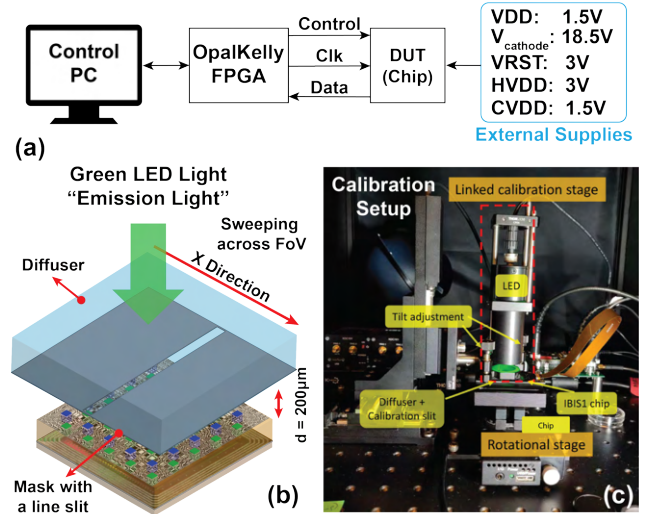


Fig. 13. (a) Schematic of the experimental setup, (b) illustration of optical setup for imager calibration, and (c) photo of the calibration setup.

underfill epoxy. Next, the μLEDs are pick-and-place flip-chip bonded using solder bumps (Step 2). In Step 3, the CMOS chip is temporary bonded on a glass carrier face-down for mechanical backside grinding and polishing via a micro-grinder tool. This in-house post-processing step results in a silicon substrate thickness of below $7.5\mu\text{m}$ with $\sim 1\mu\text{m}$ standard deviation across entire chip area. After releasing the die-thinned chip from glass carrier, we epoxy a polyimide support substrate ($\sim 50\mu\text{m}$ thick) to the backside of the chip, epoxy the optical filter (with imaging mask) to the frontside of the chip, and finally parylene coat the entire device for bio-compatibility [42]. Fig. 10b shows the cross-section of final flexible package with $< 250\mu\text{m}$ thickness.

VI. EXPERIMENTAL RESULTS

Measurements and device characterizations are presented in this section. All the measurements are done with a 40MHz reference clock leading to the 125fps frame-rate. Total chip power consumption is 40mW with 3mW and 2mW budgeted for excitation and optogenetics (for 1ms pulse-width at a 20Hz rate setting) illumination, respectively.

A. Sub-block Characterizations

Characterization of the imager's optical elements and time-gating is shown in Fig. 11. First, we characterized the spectral response of the SPAD sensor which achieves 12% photon-detection probability (PDP) at 520nm (target peak emission) with a median dark-count rate (DCR) of 26cps. The optical absorption filter provides $\sim 400\times$ ($=26\text{dB}$) rejection between 470nm and 520nm as discussed in Section V. The transmission of custom-designed interference filter at multiple angles is shown in Fig. 11b, which shows $\text{OD} > 3$ for angles below 45° .

We have also characterized the nonlinear relationship between SPAD counts and photon flux due to photon pile-up [43], [44]. While this effect is negligible in our application since the imager will only operate in the low photon-flux regime, we linearize the sensor counts to enhance imaging quality and extend the dynamic-range for other applications.

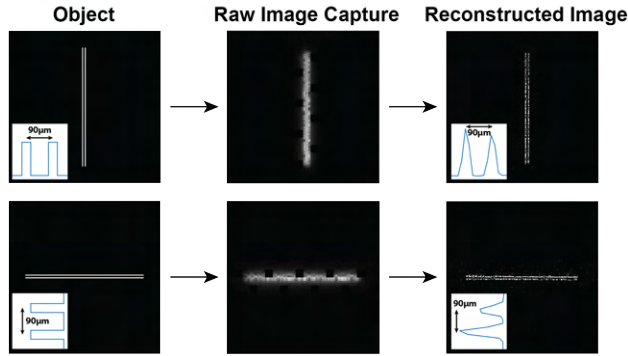


Fig. 14. Imager's resolution characterization with vertical and horizontal double-line slits (insets show median intensity across the lines).

Next, the temporal response and time-gating efficacy were evaluated by sweeping the time delay between the excitation and gating clocks while imaging Fluoresbrite YG beads (Polysciences Inc.) with $10\mu\text{m}$ diameters. Figure 11d shows the raw counts of a scene saturated with fluorescent beads illuminated via an external ps-laser incident the chip without any optical filters. The SBR plot is the ratio of the raw counts with and without the beads which show that the efficacy of TG is $\sim 15\times$ ($\sim 11.7\text{dB}$). We can also extract the beads' fluorescence lifetime ($\sim 3.6\text{ns}$), which is longer than previously reported values $\sim 2.3\text{ns}$ [45] due to the relatively long tail in the IRF response of the SPADs with an estimate full width at half maximum (FWHM) of $\sim 1.1\text{ns}$. It is known that time-gating to achieve time-correlated single-photon counting (TCSPC) in SPADs produces an longer-tail IRF to approaches based on time-to-digital converters [46], which were not implemented because of area and power constraints.

Finally, Fig. 12 shows the measured optical power density of blue and green μLEDs and the estimated target operating points for fluorescence excitation and optogenetics (providing $\sim 0.5\text{mW}/\text{mm}^2$ at $200\mu\text{m}$ in brain tissue as explained in Section II. The μLED temporal characteristics of short excitation optical pulses are measured via the SPAD detectors on the chip itself (Fig. 12b). Estimated turn-off time is $\sim 0.6\text{ns}$ given that the TG

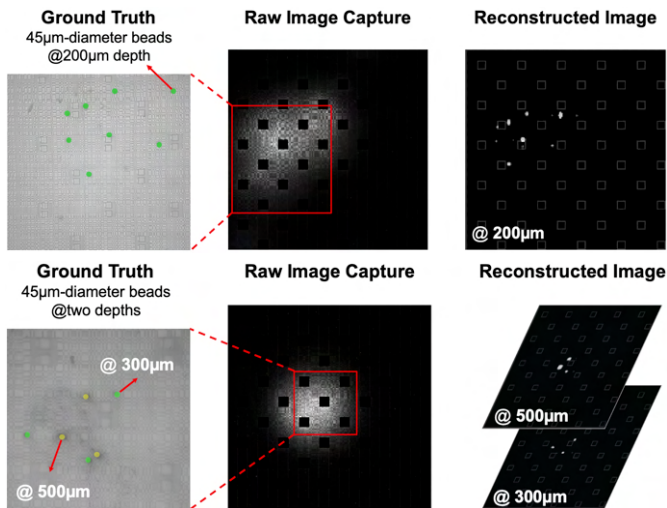


Fig. 15. Imaging sparse samples of fluorescent beads and cross-validation with confocal microscope images.

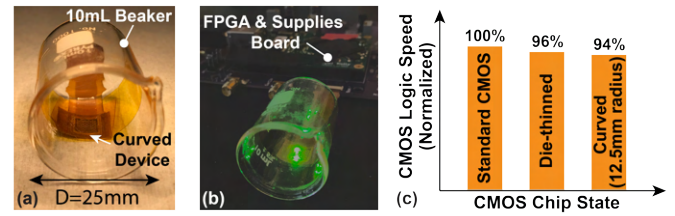


Fig. 16. (a) Photo of the mechanically flexible device wrapped around a 10mL beaker for testing, (b) functional μLEDs pulsing after bending, and (c) performance comparison of CMOS after die-thinning and bending.

imager's IRF is convolved with optical pulses in this plot. Applying a 2V reverse voltages (CVDD) using proposed μLED driver reduced the turn-off time by $\sim 0.3\text{ns}$ (Fig. 7).

B. Imager Calibration and Characterization

The experimental test setup for imaging and calibration (to estimate the separable transfer functions as explained in Section III) is shown in Fig. 13, where we used a commercial green (520nm) LED array and pass the light through a $30\mu\text{m}$ cross-hair line slit mounted to an 80° wide angle diffuser. This mimics an isotropic, fluorescent line source. The one-time calibration process is performed at the target image distances of $200\mu\text{m}$ to $500\mu\text{m}$ with a $50\mu\text{m}$ step size. After calibration, the resolution is measured by imaging a double-line slit mask with $30\mu\text{m}$ width and $60\mu\text{m}$ spacing (Fig. 14). The cross-section of the reconstructed double-line slits proves that we can achieve better than $60\mu\text{m}$ lateral resolution.

Next, a sparse sample of Fluoresbrite YG beads with $45\mu\text{m}$ diameter on a glass cover slip is imaged with our device and a confocal microscope simultaneously. Fig. 15 shows the results under $\sim 0.5\text{mW}/\text{mm}^2$ excitation intensity at the beads plane. Ground truth images are the overlap of confocal microscope image and actual bead locations. In the first experiment one sample is placed at a $200\mu\text{m}$ distance from the mask. In the second experiment, we placed two planar samples at a $300\mu\text{m}$ and $500\mu\text{m}$ distance from the mask to verify the 3D imaging capability. Beads are fully imaged and reconstructed in both

TABLE I
PERFORMANCE SUMMARY AND COMPARISON WITH PRIOR WORKS

Reference	Papageorgio, et al. [32]	Lee, et al. [33]	This Work
CMOS Technology	$0.18\mu\text{m}$	$0.18\mu\text{m}$	$0.13\mu\text{m}$
Chip Area (mm^2)	4.7×2.25	2.64×3	8×8
Supply Voltage (V)	1.8	1.8	1.5
Pixel Pitch (μm)	55	35	30
Excitation Wavelength (nm)	450	385	470
Emission Wavelength (nm)	705	540	520
PDP (or QE)	5%*	2.7%	12%
Fill-factor	28%	14.4%	5%
Resolution (μm)	220	1000^+	< 60
FoV (mm^2)	4.4×1.98	2.1×2.5	5.4×5.4
Frame-rate (fps)	20	N/R	125
Power (mW)**	3.5^+	83.8	40
Array Size	80×36	72×60	160×160
Pixels Acceptance Angle	$\pm 18^\circ$	$\pm 10^\circ$	$\pm 70^\circ$
Read-out Data-rate (Mb/s)	N/A	N/R	40
Integrated Light Source	No	No	Yes

* Estimated from figures/data, ** Illumination power not included

+ Not including off-chip ADCs

experiments with some minor artifacts. These artifacts are due to the insufficient SBR requiring further improvements to the optical filters and TG efficiency in future implementations.

The raw captures in Fig. 14 and Fig. 15 clearly show the effects of pixel “gaps” due to the placement of μ LEDs on the imager. However, we can still reconstruct the scene as explained in Section III. While reconstructed image shows some variations (e.g., peak intensities in Fig. 14) depending on the portion of missing information from the raw capture, such artifacts can be reduced in future by minimizing gap sizes (e.g., by using smaller μ LEDs). Compared to the double-line slit reconstruction (Fig. 14) which shows a few artifacts, the sparse sample in Fig. 15 is fully reconstructed without artifacts and more accurately mimics the sparsity of neural activity.

C. Mechanically Flexible Device

Finally, we wrapped the mechanically flexible device around a 10mL lab beaker with 1.25cm radius of curvature (Fig. 16) to show and evaluate the device flexibility. The flexible packaging allows for the chip and all the μ LED and I/O bond pad connections to bend without breaking, as shown in Fig. 16, where the chip is functioning and lighting up the optogenetic μ LEDs. In order to measure the impact of die-thinning and mechanical stress on electronics after bending, we measured the delay of a CMOS logic gate chain (with 16ns nominal delay), which is distributed across the chip curvature. The bar-chart shows the normalized CMOS logic speed (estimated from $1/\text{total delay}$) at each state with maximum 6% changes in the curved state. Similarly, changes in analog block (including drivers, AQC, and clocking) performance were negligible. We expect that the proposed calibration and reconstruction approach can be extended to the bended imager case with a simple geometric mapping since radius of curvature is much larger than mask feature size.

VII. CONCLUSION

Measurement’s summary and comparison with prior fluorescence imagers are presented in Table. I. We have achieved the highest resolution and largest FoV with fully integrated light-source, thanks to the computational imaging technique adopted and modified in this work.

We have demonstrated a mechanically flexible, low-power, implantable, and lens-less device for all-optical neural stimulation and recording that achieves better than $60\mu\text{m}$ resolution over a large $5.4\times 5.4\text{mm}^2$ FoV in this work. Our approach is the first step toward a fully implantable all-optical recording and stimulation brain interface device that can achieve better than cm^2 FoVs. Future generations will reduce pixel pitch and increase sensor FF by sharing SPAD’s guard-rings and simplifying in-pixel circuitry (e.g., by operating at standard VRST voltage-range which eliminates the level-shifter and thick-oxide devices). Moreover, background rejection can be further improved using semiconductor-based absorption filters and metal-dielectric interference filters. Additional power and data wireless capabilities will also simplify the flexible

packaging and make these devices more suitable for *in-vivo* applications.

ACKNOWLEDGMENT

We gratefully acknowledge TSMC for chip fabrication and support for the use of SPADs. This work was supported in part by DARPA NESD program under Contract N66001-17-C-4012 and by the National Science Foundation under Grant 1706207.

REFERENCES

- [1] V. Emiliani, A. E. Cohen, K. Deisseroth, and M. Häusser, “All-optical interrogation of neural circuits,” *Journal of Neuroscience*, vol. 35, no. 41, pp. 13917–13926, 2015, doi: 10.1523/JNEUROSCI.2916-15.2015.
- [2] K. K. Ghosh *et al.*, “Miniaturized integration of a fluorescence microscope,” *Nat. Methods*, vol. 8, no. 10, pp. 871–878, Sep. 2011, doi: 10.1038/nmeth.1694.
- [3] B. B. Scott *et al.*, “Imaging Cortical Dynamics in GCaMP Transgenic Rats with a Head-Mounted Widefield Microscope,” *Neuron*, vol. 100, no. 5, pp. 1045–1058.e5, 2018, doi: 10.1016/j.neuron.2018.09.050.
- [4] D. Aharoni and T. M. Hoogland, “Circuit Investigations With Open-Source Miniaturized Microscopes: Past, Present and Future,” *Front. Cell. Neurosci.*, vol. 13, p. 141, 2019, doi: 10.3389/fncel.2019.00141.
- [5] V. Boominathan *et al.*, “Lensless Imaging: A computational renaissance,” *IEEE Signal Process. Mag.*, vol. 33, no. 5, pp. 23–35, Sep. 2016, doi: 10.1109/MSP.2016.2581921.
- [6] J. K. Adams *et al.*, “Single-frame 3D fluorescence microscopy with ultraminiature lensless FlatScope,” *Sci. Adv.*, vol. 3, no. 12, p. e1701548, Dec. 2017, doi: 10.1126/sciadv.1701548.
- [7] A. M. Stamatakis *et al.*, “Simultaneous optogenetics and cellular resolution calcium imaging during active behavior using a miniaturized microscope,” *Front. Neurosci.*, vol. 12, no. JUL, p. 496, 2018, doi: 10.3389/fnins.2018.00496.
- [8] L. C. Moreaux *et al.*, “Integrated Neurophotonic: Toward Dense Volumetric Interrogation of Brain Circuit Activity—at Depth and in Real Time,” *Neuron*, vol. 108, no. 1, pp. 66–92, 2020, doi: <https://doi.org/10.1016/j.neuron.2020.09.043>.
- [9] K. Kampasi *et al.*, “Fiberless multicolor neural optoelectrode for in vivo circuit analysis,” *Sci. Rep.*, vol. 6, no. 1, p. 30961, 2016, doi: 10.1038/srep30961.
- [10] F. Wu, E. Stark, P.-C. Ku, K. D. Wise, G. Buzsáki, and E. Yoon, “Monolithically Integrated μ LEDs on Silicon Neural Probes for High-Resolution Optogenetic Studies in Behaving Animals,” *Neuron*, vol. 88, no. 6, pp. 1136–1148, Dec. 2015, doi: 10.1016/j.neuron.2015.10.032.
- [11] J. W. Reddy *et al.*, “High Density, Double-Sided, Flexible Optoelectronic Neural Probes With Embedded μ LEDs,” *Front. Neurosci.*, vol. 13, p. 745, 2019, doi: 10.3389/fnins.2019.00745.
- [12] C. Keum, C. Murawski, E. Archer, S. Kwon, A. Mischok, and M. C. Gather, “A substrateless, flexible, and water-

- resistant organic light-emitting diode,” *Nat. Commun.*, vol. 11, no. 1, p. 6250, 2020, doi: 10.1038/s41467-020-20016-3.
- [13] A. Steude, E. C. Witts, G. B. Miles, and M. C. Gather, “Arrays of microscopic organic LEDs for high-resolution optogenetics,” *Sci. Adv.*, vol. 2, no. 5, p. e1600061, May 2016, doi: 10.1126/sciadv.1600061.
- [14] “CREE LED Chips.” <https://cree-led.com/led-chips/products>.
- [15] A. A. Leino, A. Pulkkinen, and T. Tarvainen, “ValoMC: a Monte Carlo software and MATLAB toolbox for simulating light transport in biological tissue,” *OSA Contin.*, vol. 2, no. 3, pp. 957–972, Mar. 2019, doi: 10.1364/OSAC.2.000957.
- [16] “Appendix A: Definitions of Optical Properties,” in *Biomedical Optics*, John Wiley & Sons, Ltd, 2009, pp. 343–346.
- [17] J. Mattis *et al.*, “Principles for applying optogenetic tools derived from direct comparative analysis of microbial opsins,” *Nat. Methods*, vol. 9, no. 2, pp. 159–172, 2012, doi: 10.1038/nmeth.1808.
- [18] A. Hassibi *et al.*, “Multiplexed identification, quantification and genotyping of infectious agents using a semiconductor biochip,” *Nat. Biotechnol.*, vol. 36, no. 8, p. 738, Jul. 2018, doi: 10.1038/nbt.4179.
- [19] L. Hong, H. Li, H. Yang, and K. Sengupta, “Fully Integrated Fluorescence Biosensors On-Chip Employing Multi-Functional Nanoplasmonic Optical Structures in CMOS,” *IEEE J. Solid-State Circuits*, vol. 52, no. 9, pp. 2388–2406, 2017, doi: 10.1109/JSSC.2017.2712612.
- [20] M. Z. Lin and M. J. Schnitzer, “Genetically encoded indicators of neuronal activity,” *Nat. Neurosci.*, vol. 19, no. 9, pp. 1142–1153, 2016, doi: 10.1038/nn.4359.
- [21] U. Resch-Genger, M. Grabolle, S. Cavaliere-Jaricot, R. Nitschke, and T. Nann, “Quantum dots versus organic dyes as fluorescent labels,” *Nat. Methods*, vol. 5, no. 9, pp. 763–775, 2008, doi: 10.1038/nmeth.1248.
- [22] S. A. Hires, L. Tian, and L. L. Looger, “Reporting neural activity with genetically encoded calcium indicators,” *Brain Cell Biol.*, vol. 36, no. 1–4, pp. 69–86, Aug. 2008, doi: 10.1007/s11068-008-9029-4.
- [23] C. Richard, A. Renaudin, V. Aimez, and P. G. Charette, “An integrated hybrid interference and absorption filter for fluorescence detection in lab-on-a-chip devices,” *Lab Chip*, vol. 9, no. 10, pp. 1371–1376, 2009, doi: 10.1039/B819080A.
- [24] C. Lee *et al.*, “11.5 A 512-Pixel 3kHz-Frame-Rate Dual-Shank Lensless Filterless Single-Photon-Avalanche-Diode CMOS Neural Imaging Probe,” in *Digest of Technical Papers - IEEE International Solid-State Circuits Conference*, 2019, vol. 2019-Febru, pp. 198–200, doi: 10.1109/ISSCC.2019.8662408.
- [25] R. M. Field, S. Realov, and K. L. Shepard, “A 100 fps, Time-Correlated Single-Photon-Counting-Based Fluorescence-Lifetime Imager in 130 nm CMOS,” *IEEE J. Solid-State Circuits*, vol. 49, no. 4, pp. 867–880, 2014, doi: 10.1109/JSSC.2013.2293777.
- [26] I. M. Antolovic, C. Bruschini, and E. Charbon, “Dynamic range extension for photon counting arrays,” *Opt. Express*, vol. 26, no. 17, pp. 22234–22248, Aug. 2018, doi: 10.1364/OE.26.022234.
- [27] D. X. D. Yang and A. El Gamal, “Comparative analysis of SNR for image sensors with enhanced dynamic range,” in *Sensors, Cameras, and Systems for Scientific/Industrial Applications*, 1999, vol. 3649, pp. 197–211, [Online]. Available: <https://doi.org/10.1117/12.347075>.
- [28] T. Knöpfel and C. Song, “Optical voltage imaging in neurons: moving from technology development to practical tool,” *Nat. Rev. Neurosci.*, vol. 20, no. 12, pp. 719–727, 2019, doi: 10.1038/s41583-019-0231-4.
- [29] S. Kim, P. Tathireddy, R. A. Normann, and F. Solzbacher, “Thermal impact of an active 3-D microelectrode array implanted in the brain,” *IEEE Trans. neural Syst. Rehabil. Eng. a Publ. IEEE Eng. Med. Biol. Soc.*, vol. 15, no. 4, pp. 493–501, Dec. 2007, doi: 10.1109/TNSRE.2007.908429.
- [30] N. Antipa *et al.*, “DiffuserCam: lensless single-exposure 3D imaging,” *Optica*, vol. 5, no. 1, pp. 1–9, Jan. 2018, doi: 10.1364/OPTICA.5.000001.
- [31] V. Boominathan, J. K. Adams, J. T. Robinson, and A. Veeraraghavan, “PhlatCam: Designed Phase-Mask Based Thin Lensless Camera,” *IEEE Trans. Pattern Anal. Mach. Intell.*, vol. 42, no. 7, pp. 1618–1629, 2020, doi: 10.1109/TPAMI.2020.2987489.
- [32] E. P. Papageorgiou, B. E. Boser, and M. Anwar, “Chip-Scale Angle-Selective Imager for In Vivo Microscopic Cancer Detection,” *IEEE Trans. Biomed. Circuits Syst.*, vol. 14, no. 1, pp. 91–103, 2020, doi: 10.1109/TBCAS.2019.2959278.
- [33] C. Lee, B. Johnson, and A. Molnar, “An on-chip 72×60 angle-sensitive single photon image sensor array for lensless time-resolved 3-D fluorescence lifetime imaging,” in *2014 Symposium on VLSI Circuits Digest of Technical Papers*, 2014, pp. 1–2, doi: 10.1109/VLSIC.2014.6858427.
- [34] J. K. Adams *et al.*, “In vivo fluorescence imaging with a flat, lensless microscope,” *bioRxiv*, 2020, doi: 10.1101/2020.06.04.135236.
- [35] Y. Xue, I. G. Davison, D. A. Boas, and L. Tian, “Single-shot 3D wide-field fluorescence imaging with a Computational Miniature Mesoscope,” *Sci. Adv.*, vol. 6, no. 43, 2020, doi: 10.1126/sciadv.abb7508.
- [36] T. Kishi, H. Tanaka, Y. Umeda, and O. Takyu, “A High-Speed LED Driver That Sweeps Out the Remaining Carriers for Visible Light Communications,” *J. Light. Technol.*, vol. 32, no. 2, pp. 239–249, 2014, doi: 10.1109/JLT.2013.2292896.
- [37] S. M. Won, E. Song, J. Zhao, J. Li, J. Rivnay, and J. A. Rogers, “Recent Advances in Materials, Devices, and Systems for Neural Interfaces,” *Adv. Mater.*, vol. 30, no. 30, p. 1800534, 2018, doi: <https://doi.org/10.1002/adma.201800534>.
- [38] S. Gupta, W. T. Navaraj, L. Lorenzelli, and R. Dahiya, “Ultra-thin chips for high-performance flexible

electronics,” *npj Flex. Electron.*, vol. 2, no. 1, p. 8, 2018, doi: 10.1038/s41528-018-0021-5.

- [39] C. Banda, R. W. Johnson, T. Zhang, Z. Hou, and H. K. Charles, “Flip Chip Assembly of Thinned Silicon Die on Flex Substrates,” *IEEE Trans. Electron. Packag. Manuf.*, vol. 31, no. 1, pp. 1–8, 2008, doi: 10.1109/TEPM.2007.914217.
- [40] J. Biggs *et al.*, “A natively flexible 32-bit Arm microprocessor,” *Nature*, vol. 595, no. 7868, pp. 532–536, 2021, doi: 10.1038/s41586-021-03625-w.
- [41] E. Song *et al.*, “Flexible electronic/optoelectronic microsystems with scalable designs for chronic biointegration,” *Proc. Natl. Acad. Sci.*, vol. 116, no. 31, pp. 15398–15406, 2019, doi: 10.1073/pnas.1907697116.
- [42] C. Hassler, T. Boretius, and T. Stieglitz, “Polymers for neural implants,” *J. Polym. Sci. Part B Polym. Phys.*, vol. 49, no. 1, pp. 18–33, 2011, doi: <https://doi.org/10.1002/polb.22169>.
- [43] A. Gupta, A. Ingle, A. Velten, and M. Gupta, “Photon-Flooded Single-Photon 3D Cameras,” in *2019 IEEE/CVF Conference on Computer Vision and Pattern Recognition (CVPR)*, Jun. 2019, pp. 6763–6772, doi: 10.1109/CVPR.2019.00693.
- [44] J. Arlt, D. Tyndall, B. R. Rae, D. D.-U. Li, J. A. Richardson, and R. K. Henderson, “A study of pile-up in integrated time-correlated single photon counting systems,” *Rev. Sci. Instrum.*, vol. 84, no. 10, p. 103105, 2013, doi: 10.1063/1.4824196.
- [45] D. K. Bird, K. W. Eliceiri, C.-H. Fan, and J. G. White, “Simultaneous two-photon spectral and lifetime fluorescence microscopy,” *Appl. Opt.*, vol. 43, no. 27, pp. 5173–5182, Sep. 2004, doi: 10.1364/AO.43.005173.
- [46] D. E. Schwartz, E. Charbon, and K. L. Shepard, “A Single-Photon Avalanche Diode Array for Fluorescence Lifetime Imaging Microscopy,” *IEEE J. Solid-State Circuits*, vol. 43, no. 11, pp. 2546–2557, 2008, doi: 10.1109/JSSC.2008.2005818.



Sajjad Moazeni (M’13) received the B.S. degree in electrical engineering from the Sharif University of Technology, Tehran, Iran, in 2013, and the M.S. and Ph.D. degrees in electrical engineering and computer science from the University of California at Berkeley, Berkeley, CA, USA, in 2016 and 2018, respectively.

From 2018 to 2020, he was a Post-Doctoral Research Scientist in Bioelectronic Systems Lab at Columbia University, New York, NY, USA. He is currently an Assistant Professor of Electrical and Computer Engineering Department, at University of Washington, Seattle, WA, USA. His research interests are designing integrated systems using emerging technologies, integrated photonics, neuro and bio photonics, and analog/mixed-signal integrated circuits.



Eric H. Pollmann (S’19) received the B.S. degree in electrical engineering from the Georgia Institute of Technology, Atlanta, GA, in 2017 and the M.S. degree in electrical engineering from Columbia University, New York, NY, in 2018. He is currently pursuing the Ph.D. degree in electrical engineering at Columbia University, New York, NY. His research interests are in implantable CMOS fluorescence imagers for applications in biology and neuroscience.



Vivek Boominathan (M’19) received the bachelor’s degree in electrical engineering from the Indian Institute of Technology Hyderabad, India, in 2012, and the M.S. and Ph.D. degrees in electrical and computer engineering from Rice University, Houston, TX, USA, in 2016 and 2019, respectively. He is currently a Postdoctoral Associate at Rice University, Houston, TX, USA. His research interest lied in the areas of computer vision, computational imaging, wave optics, and machine learning.



Filipe A. Cardoso (M’11) has studied Physics Engineering at Instituto Superior Técnico (IST). During his PhD at IST and INESC-MN, he has developed magnetoresistive biosensors to detect magnetically labeled molecules. After his PhD, Filipe has continued the development of magnetoresistive sensor for both biosensors and non-destructive testing.

Filipe has further co-founded a startup company, Magnomics, aiming to push magnetoresistive biosensor technology into market, in particular animal health market. Filipe served as CTO of the company. In 2018, he has joint Prof. Ken Shepard group at Columbia University (New York, USA) as a Research Scientist where he is currently developing powering, communication and biosensing technologies for implantable devices.



Jacob T. Robinson, Jr. is an Associate Professor in Electrical & Computer Engineering and Bioengineering at Rice University, and an Adjunct Associate Professor in Neuroscience at Baylor College of Medicine. His research group uses nanofabrication technology to create devices that can manipulate and monitor neural circuit activity. He received a B.S.

in Physics from UCLA in 2003 and a Ph.D. in Applied Physics from Cornell University in 2008. After completing his Ph.D. studying silicon nanophotonics he began postdoctoral research in the Department of Chemistry and Chemical Biology at Harvard University. In 2012, he joined the ECE and BioE departments at Rice where he currently develops technologies

to better stimulate and record neural activity. Dr. Robinson is the recipient of the DARPA Young Faculty Award, the Materials Today Rising Star Award, and is a Senior Member of IEEE. He has served as co-chair of the IEEE Brain Initiative and is currently a core member of the IEEE Brain Neuroethics working group.



Ashok Veeraraghavan received the bachelor's degree in electrical engineering from the Indian Institute of Technology, Madras, Chennai, India, in 2002 and the M.S. and Ph.D. degrees from the Department of Electrical and Computer Engineering, University of Maryland, College Park, MD, USA, in 2004 and 2008, respectively. He is currently an Associate Professor of Electrical and Computer Engineering, Rice University, Houston, TX, USA. Before joining Rice University, he spent three years as a Research Scientist at Mitsubishi Electric Research Labs, Cambridge, MA, USA. His research interests are broadly in the areas of computational imaging, computer vision, machine learning, and robotics. Dr. Veeraraghavan's thesis received the Doctoral Dissertation Award from the Department of Electrical and Computer Engineering at the University of Maryland. He is the recipient of the National Science Foundation CAREER Award in 2017. At Rice University, he directs the Computational Imaging and Vision Lab.



Kenneth L. Shepard (M'91–SM'03–F'08) (Fellow, IEEE) received the B.S.E. degree from Princeton University, Princeton, NJ, USA, in 1987, and the M.S. and Ph.D. degrees in electrical engineering from Stanford University, Stanford, CA, USA, in 1988 and 1992, respectively.

From 1992 to 1997, he was a Research Staff Member and a Manager with the

VLSI Design Department, IBM Thomas J. Watson Research Center, Yorktown Heights, NY, USA, where he was responsible for the design methodology for IBM's G4S/390 microprocessors. He was the Chief Technology Officer with CadMOS Design Technology, San Jose, CA, USA, until its acquisition by Cadence Design Systems in 2001. Since 1997, he has been with Columbia University, New York, NY, USA, where he is currently the Lau Family Professor of Electrical Engineering and Biomedical Engineering and the Co-Founder and the Chairman of the Board of Ferric, Inc., New York, which commercializes technology for integrated voltage regulators. His current research interests include CMOS bioelectronics and power electronics.

Dr. Shepard has been an Associate Editor for the IEEE TRANSACTIONS ON VERY LARGE-SCALE INTEGRATION SYSTEMS, the IEEE JOURNAL OF SOLID-STATE CIRCUITS, and the IEEE TRANSACTIONS ON BIOMEDICAL CIRCUITS AND SYSTEMS.